Biochemistry **2004,** *43,* 3167−3182

Solution Structure of the Two-Iron Rubredoxin of *Pseudomonas oleovorans* Determined by NMR Spectroscopy and Solution X-ray Scattering and Interactions with Rubredoxin Reductase[†,‡]

Ashlee Perry,[∥,⊥] Winston Tambyrajah,[∥,⊥] J. Günter Grossmann,[§] Lu-Yun Lian,[#] and Nigel S. Scrutton*,[∥]

Department of Biochemistry and Centre for Chemical Biology, University of Leicester, University Road, Leicester LE1 7RH UK, Council for the Central Laboratory of the Research Councils Daresbury Laboratory, Warrington, Cheshire WA4 4AD, UK, and Department of Biomolecular Sciences, University of Manchester Institute of Science and Technology, Manchester M60 1QD, UK

Received October 8, 2003; Revised Manuscript Received January 9, 2004

ABSTRACT: Here we provide insights into the molecular structure of the two-iron 19-kDa rubredoxin (AlkG) of *Pseudomonas oleovorans* using solution-state nuclear magnetic resonance (NMR) and small-angle X-ray scattering studies. Sequence alignment and biochemical studies have suggested that AlkG comprises two rubredoxin folds connected by a linker region of ∼70 amino acid residues. The C-terminal domain (C-Rb) of this unusual rubredoxin, together with ∼35 amino acid residues of the predicted linker region, was expressed in *Escherichia coli*, purified in the one-iron form and the structure of the cadmium-substituted form determined at high-resolution by NMR spectroscopy. The structure shows that the C-Rb domain is similar in fold to the conventional one-iron rubredoxins from other organisms, whereas the linker region does not have any discernible structure. This tandem "flexible-folded" structure of the polypeptide chain derived for the C-Rb protein was confirmed using solution X-ray scattering methods. X-ray scattering studies of AlkG indicated that the 70-amino acid residue linker forms a structured, yet mobile, polypeptide segment connecting the globular N- and C-terminal domains. The X-ray scattering studies also showed that the N-terminal domain (N-Rb) has a molecular conformation similar to that of C-Rb. The restored molecular shape indicates that the folded N-Rb and C-Rb domains of AlkG are noticeably separated, suggesting some domain movement on complex formation with rubredoxin reductase to allow interdomain electron transfer between the metal centers in AlkG. This study demonstrates the advantage of combining X-ray scattering and NMR methods in structural studies of dynamic, multidomain proteins that are not suited to crystallographic analysis. The study forms a structural foundation for functional studies of the interaction and electron-transfer reactions of AlkG with rubredoxin reductase, also reported herein.

The rubredoxins are a family of non-heme iron proteins whose active sites comprise an iron atom tetrahedrally coordinated to four cysteine residues (*1*). Rubredoxin is used as an electron donor in the superoxide reductase electron-transfer chain in anaerobic organisms (*2*). An additional role as a cofactor of terminal oxidase in *Desulfovibrio gigas* (*3*) and in hydrogen oxidation in *Azotobacter vinelandii* (*4*) has also been described. The first eukaryotic rubredoxin was identified recently and found to be associated with photosystem II of the unicellular alga *Guillardia theta* (*5*, *6*). In aerobic bacteria, rubredoxins act as electron carriers in the alkane hydroxylation system (*7*, *8*), and the electron-transfer reactions have been investigated in detail for the rubredoxin (AlkG)[1] of *Pseudomonas oleovorans* (*9*). In the multiprotein system responsible for the hydroxylation of alkanes, AlkG shuttles electrons from a specific NADH-dependent rubredoxin reductase (RR) to the membrane-bound, di-iron alkane hydroxylase (*10*, *11*).

The 19-kDa rubredoxin of *Ps. oleovorans* is over three times the size of a typical rubredoxin. Sequence alignments suggest that the gene [*alk* G; (*10*)] for *Ps. oleovorans* rubredoxin encodes two rubredoxin-type domains separated by a linker of approximately ∼70 amino acid residues; the *alk* G gene is thought to be the product of a gene duplication event. The secondary and tertiary structures of the rubredoxins are highly conserved across the different organisms; these structures have been studied extensively by NMR spectroscopy [*Clostridium pasteurianum* (*12*), *Pyrococcus furiosus* (*13*)] and X-ray crystallography [*D. sulfuricans* (*14*),

---

[†] This work was funded by the UK Engineering and Physical Sciences Research Council, the Biotechnology and Biological Sciences Research Council, and the Lister Institute of Preventive Medicine. N.S.S. is a Lister Institute Research Professor. W.S.T. was funded by the Krebs Memorial Scholarship from the Biochemical Society, UK.

[‡] Coordinates for C-Rb have been deposited in the protein database (PDB ID code: 1S24).

* Corresponding author: Professor N. S. Scrutton. Telephone +44 116 223 1337; fax +44 116 252 3369; e-mail nss4@le.ac.uk; Professor L-Y Lian, e-mail lu-yun.lian@umist.ac.uk.

[⊥] The first two named authors contributed equally to this work.

[∥] University of Leicester.

[§] Council for the Central Laboratory of the Research Councils Daresbury Laboratory.

[#] University of Manchester Institute of Science and Technology.

[1] Abbreviations: AlkG, full-length rubredoxin of *Ps. oleovorans*; C-Rb, C-terminal domain of *Ps. oleovorans* rubredoxin; N-Rb, N-terminal domain of *Ps. oleovorans* rubredoxin; 1Fe-Rb, AlkG with iron bound only to the C-terminal domain; 2Fe-Rb, AlkG with iron bound to the N- and C-terminal domains; RR, rubredoxin reductase; NOESY, nuclear Overhauser enhancement spectroscopy; DQF-COSY, double quantum filtered correlated spectroscopy; TOCSY, total correlated spectroscopy.

10.1021/bi035817u CCC: $27.50

D. gigas (*15*), *D. vulgaris* (*16*), *C. pasteurianum* (*17*), and *P. furiosus* (*18*)]. Most rubredoxins possess two motifs responsible for binding a single iron, which comprise the sequence Cys-X-X-Cys-Gly. This motif is found in the C-Rb domain of AlkG, but in the N-Rb domain the glycine residue in this consensus region is replaced by asparagine (in the first iron-binding motif) and alanine (in the second motif). Biochemical studies have confirmed that AlkG contains two iron atoms per molecule and that there are two discrete binding sites for iron (*8*, *19*).

To address the functional reasons for the existence of two rubredoxin domains in AlkG, we have carried out biochemical and structural studies on the full-length and truncated proteins. We recently reported the genetic excision and purification of the N-Rb and C-Rb domains of AlkG and studies of their spectroscopic properties (*20*). The C-Rb domain is redox-active and mediates electron transfer from its physiological electron donor RR to partner proteins (*9*, *20*, *21*). The absorption and circular dichroism spectra of the iron- and cadmium-substituted C-Rb domain are similar to those reported for iron- and cadmium-substituted *D. gigas* rubredoxin (*22*). Attempts to express the N-Rb domain alone in *Escherichia coli* were unsuccessful, but it was possible to isolate this domain by cleavage of a full-length variant that contained an engineered factor Xa proteolysis site in the putative interdomain linker (*20*). The absorption spectrum of this proteolytically released domain revealed properties typical of the conventional one-iron rubredoxins. The N-Rb domain is folded and redox-active, but is much less stable than the isolated C-Rb domain (*20*). Given the high sequence identity and the similar metal-binding characteristics, the N-Rb and C-Rb domains are inferred to be structurally related, and are probably the result of gene duplication. Here, we present the high-resolution NMR structure of the stable, cadmium-substituted C-Rb domain, which like other Cd-substituted rubredoxins is essentially isostructural with the physiological iron form (*23*). We also present low-resolution structural studies of AlkG and the C-Rb domain using small-angle X-ray scattering methods. These studies provide evidence for a dynamic, multidomain protein whose redox domains are positioned to enable electron exchange between the metal centers. Our work demonstrates the utility of combining solution NMR and X-ray scattering methods to obtain structural information for intact, functional forms of multidomain proteins with linker region(s). Proteins of this class are not normally amenable to high-resolution structural studies using conventional crystallographic methods. The structural studies provide a firm foundation for functional analysis of the two domains. We also report studies of the interaction of C-Rb and N-Rb with RR and kinetics of electron transfer. Our data suggest that the C-Rb domain is the primary electron acceptor of RR, consistent with in vivo studies with truncated rubredoxin proteins.

EXPERIMENTAL PROCEDURES

Purification of Rubredoxins. Purification of AlkG containing iron in the C-Rb domain only, or containing iron in the N-Rb and C-Rb domains, was as described previously (*23*). Expression and purification of the isolated C-Rb domain were as described by Perry et al (*23*) and the bound iron replaced by cadmium as described previously (*23*). Previous attempts to express the isolated N-Rb domain have been unsuccessful, but the domain can be isolated by Factor Xa cleavage of an engineered AlkG protein (AlkG-His) that contains an internal Factor Xa cleavage site in the interdomain linker and a histidine extension at the C-terminal end of the C-Rb domain (*20*). Isolation of the N-Rb domain was using a modified procedure to that described by Perry et al (*20*). AlkG-His was partially purified as described (*20*) and was subsequently applied to a metal chelating Sepharose-FF column [25 mL bed volume, 16 mm × 20 cm, charged with 100 mM nickel sulfate (50 mL) and washed with deionized water (250 mL) and equilibrated with 100 mM Tris-HCl buffer, pH 7.5, containing 1.0 M KCl and 5 mM imidazole (buffer A)] to obtain pure AlkG-His. The column was washed with buffer A (150 mL), and AlkG-His was eluted with elution buffer (100 mM Tris-HCl, pH 7.0, containing 1.0 M KCl and 1.0 M imidazole). Fractions containing AlkG-His were pooled and the protein was dialyzed exhaustively against 100 mM Tris-HCl buffer, pH 7.5 at 4 °C. AlkG-His was cleaved by incubating the protein with Factor-Xa (5 units/1.0 mg of protein) at room temperature (~22 °C) with gentle stirring for 24 h. This cleaved protein was purified using a metal chelating Sepharose-FF column (25-mL bed volume, 16 mm × 20 cm) and the conditions described for purification of AlkG-His. Fractions (1 mL) were collected during loading of the protein on the column to obtain the N-Rb domain in the iron-free form. Buffer exchange was by exhaustive dialysis against 100 mM potassium phosphate buffer, pH 7.5.

Incorporation of Iron into Rubredoxins. The method used to reconstitute the N-Rb domains in AlkG and the isolated N-Rb domain with iron was modified from that described by Lee et al (*23*). Protein was precipitated at room temperature with trichloroacetic acid [TCA; final concentration of 10% (w/v)]. The precipitate was harvested by centrifugation and subsequent steps were performed in an anaerobic glovebox (Belle Technology Ltd). The protein pellet was dissolved (~5 mg/mL) in 500 mM Tris base containing 500 mM 2-mercaptoethanol and maintained at 25 °C for 3 h in the glovebox. Protein was then reprecipitated with TCA [final concentration 10% (w/v)] and harvested by centrifugation. The protein pellet was redissolved in 500 mM Tris base containing a 5-fold molar excess of ferrous ammonium sulfate over protein. After incubation for 1 h at 4 °C, the solution was exposed to air and the protein was desalted using a Sephadex-G25 column (Whatman) equilibrated with 100 mM potassium phosphate buffer, pH 7.5, to remove excess ferrous ammonium sulfate. For the isolated N-Rb domain the final refolding buffer also contained glycerol (20% v/v).

Purification of Rubredoxin Reductase. Purification of RR was from *E. coli* strain TG1 transformed with plasmid pKRRV, using ampicillin as the selection antibiotic (*9*). Production of cell lysates and fractionation with ammonium sulfate were as described previously (*9*), but to improve the yield of RR the following chromatography steps were employed in this work. The protein contained in 20 mM potassium phosphate buffer, pH 7.5 (buffer B) was applied to a Q-Sepharose-FF column (50 mm × 20 cm) equilibrated with buffer B and washed (900 mL) with buffer B. Protein was eluted with a gradient of KCl contained in buffer B plus glycerol (20% v/v). The gradient was increased from 0 to 140 mM KCl (300 mL); the KCl concentration was then maintained at 140 mM KCl (150 mL) and then increased from 140 to 200 mM (300 mL) to elute the protein. Fractions containing RR were pooled and dialyzed exhaustively against buffer A at 4 °C. The dialyzed protein was then applied to a Q-Sepharose-HP column (26 mm × 20 cm) and rechromatographed as described above. Fractions containing pure RR were pooled and dialyzed exhaustively against buffer A at 4 °C. The specific activity of purified RR (91 units/mg) compares favorably with values reported elsewhere [82 units/mg (*24*) and 86 units/mg (*9*)].

Protein Concentration and Stability Assays. The concentration of the rubredoxins was determined from absorbance measurements at 498 nm [1Fe-Rb and C-Rb ($\epsilon_{498} = 6300$ M^{-1} cm^{-1})], 486 nm [N-Rb ($\epsilon_{486} = \sim 5000$ M^{-1} cm^{-1})], and 494 nm [2Fe-Rb ($\epsilon_{498} = 10\,600$ M^{-1} cm^{-1})]. Values for extinction coefficients were taken from published work (*20*, *23*, *25*). The extinction coefficient for N-Rb is approximate owing to the lability of the bound iron in the refolded domain (*20*). The concentration of RR was determined from absorbance measurements at 450 nm [$\epsilon_{450} = 11\,100$ M^{-1} cm^{-1} (*24*)]. The stabilities of 2Fe-Rb, 1Fe-Rb, C-Rb, and N-Rb were monitored by absorption measurements at 486 nm where the protein absorbs strongly owing to the presence of the bound iron. Proteins were maintained at 20 °C in 100 mM Tris HCl buffer, pH 7.3, in the absence or presence of glycerol (0, 10, 20, and 50% v/v). The stability of RR was monitored by the increase in FAD fluorescence emission at 530 nm (excitation 458 nm) following release of FAD from the protein using a Cary-Varian eclipse fluorescence spectrophotometer. RR was maintained at 20 °C in 100 mM Tris-HCl buffer, pH 7.3, in the absence or presence of glycerol (20% v/v). Studies were extended to include 2Fe-Rb, 1Fe-Rb, C-Rb, and N-Rb in RR stability assays; these studies were performed in the absence of glycerol, except with N-Rb where glycerol was included (20% v/v).

NMR Spectroscopy. The ^{1}H NMR spectra of the C-Rb domain were recorded with a Bruker DMX-500 spectrometer. The NMR sample (10 mM Cd-substituted C-Rb domain in 20 mM potassium phosphate buffer, pH 7.6) was made up in either $H_2O/^2H_2O$ (9:1, v/v) or $H_2O/^2H_2O$ (1:99, v/v). Spectra were recorded at 298 and 313 K. Proton chemical shifts were referenced to 2,2-dimethylsilapentane-5-sulfonic acid at 0 ppm. Homonuclear two-dimensional double-quantum-filtered COSY, TOCSY, and NOESY data were acquired using standard pulse sequences. All spectra were measured in phase-sensitive modes. COSY data matrices were 4096 × 512, TOCSY and NOESY data matrices were 2048 × 512 real-time domain data points. All 2D data were processed with zero-filling in both the F_1 and F_2 dimensions.

Restraints for Structure Calculations. Distance restraints were derived from NOESY data obtained at a mixing time of 100 ms. The NOE cross-peaks were selected both manually and automatically by computer-assisted methods; the manual selection was necessary to overcome anomalous peak identification owing to severe peak overlap. Three cross-peak lists were used: two generated automatically from datasets obtained at 298 and 310 K, and one manually from data at 298 K. The NOE peak lists together with the chemical shift table were converted into ARIA/X-PLOR format (*26*). Seven hydrogen bonds were identified using the data from the amide exchange experiment. No angular restraints were used in the calculation of the structure owing to severe overlap of many of the cross-peaks, making any derived angular restraints highly unreliable. Nevertheless, good structural convergence in the absence of angular restraints was obtained.

Structure Calculation. No structural restraints were placed on residues 85−118, since resonances from this region could not be assigned. We concluded that this region, which forms half the linker region between the two rubredoxin domains in full-length AlkG, was largely unstructured. To reduce processing time with respect to the simulated annealing protocol, only restraints involving residues 118−173 were included in the calculations. Structures were generated by implementing the ARIA suite of programs (*27*). The initial structure of the cadmium-substituted C-Rb domain was modeled using MODELLER-4 (*28*) based on the high-resolution crystal structures of *C. pasteurianum* (*17*), *D. gigas* (*15*), *D. vulgaris* (*16*), *and P. furiosus* (*18*) rubredoxins. The modeled structures were used for the initial structure-based assignments of ambiguous NOE cross-peaks (with a generous distance cutoff of approximately 7 Å). The starting structure of C-Rb was refined against NMR-derived constraints using the ARIA program, which is capable of dealing with ambiguously assigned distance constraints (*26*). In the first round of ARIA calculation, all peaks whose chemical shifts corresponded to assigned protons were converted into restraints; a set of 20 structures was obtained. Subsequent iterations began by ordering the structures from the previous iteration for calibration and restraint selection (the violation tolerance is reduced to 0.5 Å after the first iteration, ambiguously assigned NOE peaks were resolved, and the corresponding restraint(s) discarded based on structures produced from experimentally derived data). The 10 conformers with the lowest final CNS target function values were energy-minimized in a water shell as a part of standard ARIA procedure (*29*). All the NOE restraints used for the structure calculation were self-consistent and produced a converged set of final structures, thus validating the approach in using modeled structures for the initial assignments of the NOEs. The final structures were analyzed with the PROCHECK program (*30*).

Solution X-ray Scattering. Data were collected in one session with the low angle scattering camera on station 2.1 at the Synchrotron Radiation Source (SRS), Daresbury, UK, using a position-sensitive multiwire proportional counter. At the sample-to-detector distance of 1.25 m and the X-ray wavelength of $\lambda = 1.54$ Å, a momentum transfer interval of $0.005 \leq s \leq 0.087$ Å^{-1} was covered. The modulus of the momentum transfer was defined as $s = 2 \sin \Theta/\lambda$, where 2Θ was the scattering angle. The *s*-range was calibrated using an orientated specimen of wet rat tail collagen (based on diffraction spacing of 670 Å). Samples were contained in a brass cell holding a Teflon ring sandwiched by two mica windows that defined a sample volume of 120 μL and a thickness of 1.5 mm. The brass cell was maintained at 18 °C during data acquisition. Buffer and sample were measured in alteration, each in a frame of 60 s (amounting to total measuring times between 15 and 60 min, dependent upon the sample concentration and changes monitored on-line during experiments).

Interpretation of X-ray Scattering Data. Reduction and analysis of scattering data was performed as described previously (*31*). Radius of gyration (R_g), forward scattering intensity (I_o), and the intraparticle distance distribution function $p(r)$ were calculated from the experimental scattering data using the indirect Fourier transform method as implemented in the program GNOM (*32*). Relative I_o/c values (c = sample concentration) gave the relative molecular weight of the protein samples when referenced against a suitable standard (bovine serum albumin was used with a known molecular mass of 66 kDa). The maximum linear dimension D_{max} of the particle could be evaluated owing to the characteristic of $p(r)$. The volume V of the particle was calculated from the Porod invariant (*33*) and a correction factor, taking into account the limited experimental scattering range (*34*).

At low scattering angles ($s < 0.04$ Å^{-1}) the shape scattering (i.e., the scattering from the molecular boundary which is defined by a uniform mass density) dominates. The latter can be exploited to reconstruct a molecular envelope from the scattering profile using, for example, the spherical harmonics method developed by Svergun et al. (*31*). However, due to the relatively small size, the expected molecular flexibility and conformational anisometry of the rubredoxin molecules, significant contributions from molecular inhomogeneities will add to the scattering signal in the measured scattering interval (in particular for $s > 0.04$ Å^{-1}). Therefore, ab initio shape reconstructions were carried out based on simulated annealing with a set of dummy spheres each representing a residue of the polypeptide chain (*32*). As long as reliable scattering data beyond the traditional small-angle scattering regime is available ($s \geq 0.05$ Å^{-1}), this method provides considerably more consistent and higher resolution models than previous methods (such as the spherical harmonics approach). Several shape reconstructions for each of the scattering profiles (C-Rb and full-length rubredoxins) were carried out to evaluate the uniqueness of the restored conformations. Superimposition of low- and high-resolution protein models was performed with the program SUPCOMB (*35*). Individual models of C-Rb (NMR structure) and N-Rb (model based on the C-Rb NMR structure) were fitted into the reconstructed shapes deduced from the scattering data. Concerning the shape model, it was necessary before the fitting to separate all spheres corresponding to the two individual domains and to exclude the connecting linker segment.

Fluorescence Quenching and Complex Assembly. Complex formation between RR and the different rubredoxins (AlkG and its domains) was analyzed by the quenching of RR-bound FAD fluorescence (excitation 458 nm; emission 530; 20 °C). The rubredoxins (120 μM stock solution) were added in small aliquots (5−20 μL) to a solution of RR (4 μM) and incubated to allow equilibration (typically 1 min) prior to measuring the FAD fluorescence. Measurements were obtained for 0 to 25 molar ratios of the rubredoxins and RR. To account for the inner filter effect, control experiments were performed using FAD solution (4 μM) titrated with the rubredoxins. Also, RR (4 μM) was titrated with buffer to correct for dilution effects. Binding experiments were performed in 20 mM Tris-HCl buffer, pH 7.3. The effect of ionic strength on the binding of 1Fe-Rb to RR was also investigated using KCl (0 to 1.0 M). Fluorescence data were collected using a Cary-Varian eclipse fluorescence spectrophotometer and were fitted to eq 1 to obtain the dissociation constant (K_d) of the protein−protein complex:

$$\Delta F = \frac{\Delta F_{max}}{2Et}[(Lt + Et + K_d) - (\{Lt + Et + K_d\}^2 - \{4Lt \times Et\})^{(1/2)}] \quad (1)$$

In eq 1, ΔF is the change in fluorescence signal, ΔF_{max} is the maximum change in fluorescence signal, Lt is the total concentration of the ligand (i.e., rubredoxin), and Et is the concentration of binding sites in the protein.

Steady-State Kinetic Methods. Steady-state assays of rubredoxin-mediated reduction of cytochrome *c* by RR was performed essentially as described previously (*24*), but with glycerol (20% v/v) included in the reaction mix. The reaction mixture (1 mL) comprised 50 mM Tris-HCl buffer, pH 7.8, containing glycerol (20% v/v), 83 μM cytochrome *c* (horse heart), RR (2 μM), NADH (0.3 mM), and rubredoxin (0−200 nM). The reaction was initiated by adding NADH and the absorbance change was followed at 550 nm at 30 °C. All assays were performed using a Jasco J-530 spectrophotometer and monitored at 550 nm (ϵ_{550} = 21 000 M^{-1} cm^{-1}). Data analysis was performed using the standard Michaelis−Menten equation.

Stopped-Flow Methods. Stopped-flow kinetic experiments were performed using an Applied Photophysics SX.17MV reaction analyzer capable of single or multiple wavelength, time-dependent measurements using single or sequential mixing modes in absorbance or fluorescence mode. Reactions were performed at their specified experimental temperatures. Single wavelength or fluorescence emission data were fitted by nonlinear least-squares regression analysis using Spectrakinetics software (Applied Photophysics). Data (average of at least five reaction transients) were analyzed using either single or double exponential expressions. The kinetics of complex formation were monitored by following the quenching of FAD fluorescence from the FAD cofactor in RR on binding different rubredoxin forms. Component proteins were contained in 20 mM Tris-HCl buffer, pH 7.3, containing 20% glycerol, and reactions were performed at 5 or 25 °C. The FAD fluorophore was excited at 458 nm; fluorescence emission was measured using an edge-pass filter (Ealing optics) placed between the reaction cell and the photomultiplier. Similar kinetic transients were also obtained in 50 mM potassium phosphate buffer, pH 7.0 and 20% glycerol (i.e., the buffer used in previous stopped-flow studies of electron transfer; see below). Sequential mixing stopped-flow methods for investigating the rates of electron transfer from reduced RR to 1Fe-Rb and 2Fe-Rb have been described elsewhere (*9*), and these methods were used to investigate rates of electron transfer to the C-Rb and N-Rb domains. Reactions were performed in 50 mM potassium phosphate buffer, pH 7.0 and 20% (v/v) glycerol at 5 °C and involved the mixing of RR (2.5 μM) with half-stoichiometric NADH to effect reduction of RR. Following a 5 s aging time, the reduced RR was mixed with either C-Rb (0−75 μM) or N-Rb (0−100 μM). Reduction of C-Rb and N-Rb was observed at 530 nm and transients were monophasic. Similar experiments were performed with photodiode array detection to confirm that the spectral changes observed on reduction of C-Rb and N-Rb by RR were similar to those observed previously using 1Fe-Rb and 2Fe-Rb (*9*).

RESULTS

Proton Resonance Assignments and Structure Determination of the C-Terminal Rubredoxin Domain (C-Rb). The cadmium-substituted C-Rb domain was stable and obtained in high yield when expressed in unlabeled 2YT rich media.

MASYKCPDCN YVYDESAGNV HEGFSPGTPW HLIPEDWCCP DCAVRDKLDF
MLIESGVGEK GVTSTHTSPN LSEVSGTSLT AEAVVA*PTSL EKLPSADVKG*
QDLYKTQPPR SDAQGGKAYL KWICITCGHI YDEALGDEAE GFTPGTRFED
IPDDWCCPDC GATKEDYVLY

FIGURE 1: Complete sequence of the AlkG from *Ps. oleovarans*. The C-Rb domain used for the structural studies is shown in italics with the rubredoxin fold indicated by underlining.

However, only extremely low yields of this protein were obtained in either isotopically labeled minimal media or algal lysates. We were, additionally, not able to obtain sufficient amounts of the N-Rb protein in a stable form for structural studies, consistent with earlier reports on the poor stability of this domain (*20*). The solution structure of the C-Rb domain was therefore determined using conventional ^{1}H NMR spectra (*20, 36*). The different types of amino acid residues were identified and assigned via through-bond (DQF-COSY and TOCSY) and sequential interresidue through-space connectivities (NOESY). Cadmium substitution was used to overcome paramagnetic line-broadening effects on resonances from residues that are in close proximity to the metal center in iron-containing protein. Similar paramagnetic effects have also been observed for iron-containing rubredoxin from *P. furiosus* (*37*). We had previously shown that the C-Rb domain adopted the same conformation when it existed either as an independent domain or when present in full-length rubredoxin (*20*). Resolved resonances in the full-length protein (AlkG) appeared approximately as a simple summation of the signals from each single domain, suggesting that there were no major structural interactions between the two domains.

The expression construct used to make the C-Rb domain encodes one-half of the interdomain linker and the C-terminal iron-binding domain (i.e., residues 85−173; Figure 1). There are 87 amino acids in total, 39 residues with unique spin systems (eight Gly, six Ala, four Ile, six Thr, six Leu, seven Pro, and two Val), 28 residues with AMX spin systems (corresponding to the $H^{\alpha}-H^{\beta 2},H^{\beta 3}$ of ten Asp, five Cys, five Tyr, three Ser, two Phe, two Trp, and one His) and 20 residues with "longer" spin systems (eight Glu, seven Lys, three Gln, and two Arg).

In the fingerprint region of the DQF-COSY spectrum, 64 out of the expected 80 resonances were observed, with 44 being well-resolved and 20 occurring in a heavily overlapped region between 7.5 and 8.5 ppm (Supporting Information). Many of the remaining missing peaks were later identified in the TOCSY and NOESY spectra. TOCSY spectra at long mixing times (80 ms) enabled delineation of many of the spin systems. The NOESY spectra were used to aid the assignments of the $H^{\beta 2},H^{\beta 3}$ protons of the aromatic residues. The sequence-specific resonance assignment was achieved from the NOESY spectrum (100 ms) by standard procedure, using interresidue sequential H^N-H^{α} and H^N-H^N NOE connectivities. Segments of polypeptides were identified from a combination of the TOCSY and NOESY experiments. All the residues whose resonances were assigned fall within the region predicted, by sequence alignments, to form the structured cadmium binding domain (residues 118−173; Figure 1). Some resonances from the folded region were "buried" under the intense, poorly resolved resonances, thereby precluding their assignments. Since all the well-dispersed amide resonances are assigned to residues from the folded rubredoxin domain, most of these intense, overlapping amide resonances must originate from the linker region. The poor resolution and significant lack of sequential NOE connectivities meant that these signals could not be assigned using homonuclear ^{1}H NMR experiments, which in turn implies that the linker region in C-Rb is mobile and largely unstructured. The difficulties encountered in expressing this domain in labeled media to produce ^{15}N-labeled C-Rb precluded the acquisition of ^{15}N relaxation data for further dynamics analysis of this region of the protein. A near complete list of the assignments is given in Supporting Information. Because of the significant resonance overlap in the aliphatic region of the 2D homonuclear spectra, many of the resonances from proline residues and some aspartate side-chains could not be assigned; these include residues around the redox center (Pro158, Asp153, and 159). Although in principle this could have been resolved using isotopically labelled protein, as mentioned earlier, it was difficult to produce sufficient quantities of labeled C-Rb. A summary of the short-range NOEs involving NH and $C^{\alpha}H$ is given in Figure 2A. Regular secondary structure elements of β-sheet and tight turn, as shown in Figure 2B, were identified from a qualitative interpretation of the NOEs and amide proton exchange rates.

The three-dimensional structure of C-Rb (encompassing residues 118−173) was determined in aqueous solution at pH 7.6 at 25 °C, using data acquired for C-Rb residues 87−173 (i.e., encompassing the linker region). However, since the first 32 amino acids were deemed to be essentially unfolded, these residues were not included in the structure calculations. A total of 900 restraints were used, which approximates to 16 restraints per residue. The structures were generated with metal ligation from the start, since the cysteine residues in the metal binding motif had been shown to be liganded to the cadmium center using ^{113}Cd-^{1}H HSQC experiments (*20*). Restraints were used to enforce the Cd−S coordinate bond for cysteines 124, 127, 157, and 160 in the metal binding site; the Cd−S distance was restrained by 2.5 ± 0.05Å, and the Cd−C^{β} by 3.5 ± 0.25Å (C^{β} refers to the β carbon of the cysteine residue) (*38*). The use of two distance restraints for each cysteine residue ensures that the S−Cd−S angle remains within allowed limits. The RMSD values for the backbone and heavy atoms relative to the mean coordinates were 0.71 ± 0.1 and 1.29 ± 0.1 Å, respectively. A detailed analysis of the C^{α} RMSD and the distribution of restraints indicate a good correlation between the two (Figure 3). The C^{α} RMSD is high in areas with a low number of restraints, and is highest among the core residues for Pro 152 and Asp153, which lack restraints. The high conservation of the residues around the redox center between C-Rb and the rubredoxins whose crystal structures were used to provide the initial C-Rb model structure, together with the use of Cd−S restraints enabled the architecture around the redox center to be preserved despite this lack of restraints. The areas of lowest C^{α} RMSD are those involved in β-sheet formation.

The final ensemble of structures is displayed in Figure 4A, showing the backbone superimposition of 20 structures and a ribbon representation is shown in Figure 4B. The quality of the obtained structures was checked with PROCHECK-NMR (*30*). Statistics of the ensemble are given in Table 1. The number of restraints used to generate the structures and the RMSD values obtained for the final

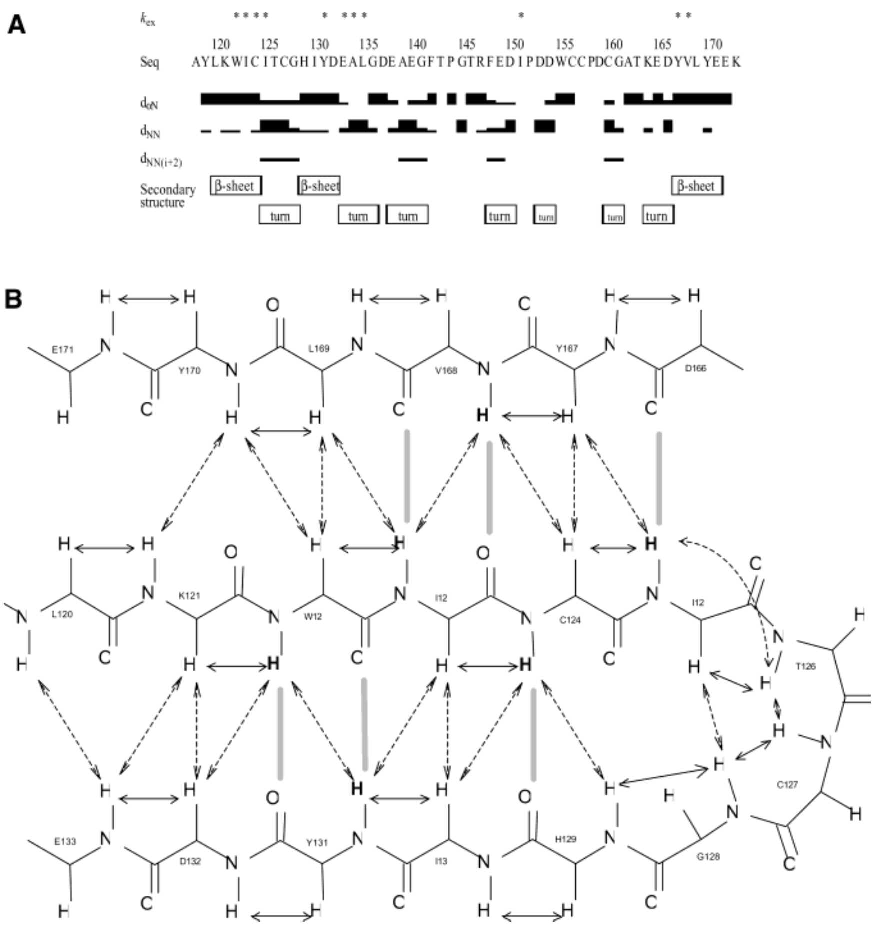

FIGURE 2: (A) Summary of sequential $H^{\alpha}-H^{N}$, $H^{N}-H^{N}$, and $H^{N}-H^{N(i+2)}$ connectivities observed in the NOESY spectra of the C-Rb domain. The thickness of the bar reflects the relative intensity of the cross-peak observed. Secondary structure elements are shown at the bottom. Above the amino acid sequence, the asterisk indicates residues with slow hydrogen exchange rates at the backbone amide after 24 h incubation at room temperature in D_2O. (B) Schematic representation of the three-stranded antiparallel β-sheet observed in the C-Rb domain. Double-headed arrows indicate observed NOE connectivities. Slowly exchanging H^N protons involved in hydrogen bonds are shown in bold, with hydrogen bonds shown as gray bands.

structures compare well with the NMR structure determination of the rubredoxin of *P. furiosus* (*39*).

The overall structure of C-Rb is similar to other rubredoxin structures determined by NMR and X-ray crystallography (*15*−*17*). The structure comprises a three-stranded antiparallel β-sheet, formed from residues Leu 120−Ile 125, His 129−Glu 133, and Tyr 167−Glu 171, and a number of tight turns involving residues Ile 125−Gly 128, Glu 33−Gly 136, Glu 138−Phe142, Phe 148−Ile 151, Asp 159−Ala 162, Lys 164−Tyr 167. Residues Arg 148−Leu 152 and Thr 164−Tyr 168 show helical characteristics, as revealed by analysis of the NMR ensemble by PROCHECK-NMR (*30*). The NOE patterns did not reveal the presence of helical regions, owing possibly to their relatively short length (two and three residues). Comparative backbone RMSD values with the high-resolution crystal structures of other rubredoxins are given in Table 2, showing the high level of similarity between these structures and C-Rb.

It is worthwhile comparing the NMR features of C-Rb that are consistent with the putative rubredoxin structure. In all the NMR structures of rubredoxins, the chemical shifts of the methyl groups of comparable aliphatic residues, Ile 151 (C-Rb), Leu 32 (*P. furiosus*) and Ile 33 (*C. pasteurianum*), exhibit large upfield shifts of −1.23, −1.61, and −1.29 ppm, respectively. In addition, in C-Rb there is an extensive network of NOEs involving Tyr 131, Phe 148, Ile 151, and Trp 155; equivalent networks have also been previously found in *P. furiosus* and *C. pasteurianum* rubredoxins involving Tyr 12, Phe 29, Leu 32, Trp 26 (*P. furiosus*), and Tyr 13, Phe 30, Ile 33, and Trp 37 (*C. pasteurianum*). Similar hydrophobic cores exist in all these structures; the one for C-Rb determined in this paper is shown in Figure 4C. Unambiguous nonsequential restraints involving these hydrophobic residues constitute 39% of the medium- and long-range restraints used for the calculation of the NMR structures here.

The secondary structure elements of a three-stranded antiparallel β-sheet with tight turns at the ends of the β-sheets in C-Rb, as identified by the short-range NOEs and amide proton exchange rates, and subsequently shown in the calculated structure, are similar to those observed in the NMR studies of *P. furiosus* and *C. pasteurianum* rubredoxins. These encompass residues Ala 1−Lys 6, Tyr 10−Glu 14, Phe 48−Glu 52 of *P. furiosus* rubredoxin; residues Lys 3−Cys 6, Tyr 11−Asn 14, Phe 49−Val 52 of *C. pasteurianum* rubredoxin; and residues Leu 120−Ile 125, His 129−Glu 133, Tyr 167−Glu 171 of C-Rb.

Solution X-ray Scattering of the C-Rb Domain. X-ray scattering data analysis was performed on C-Rb at protein concentrations of 1 and 12.8 mg/mL. The collection of scattering profiles at low and high concentrations allows one to distinguish between interparticle effects (owing to the

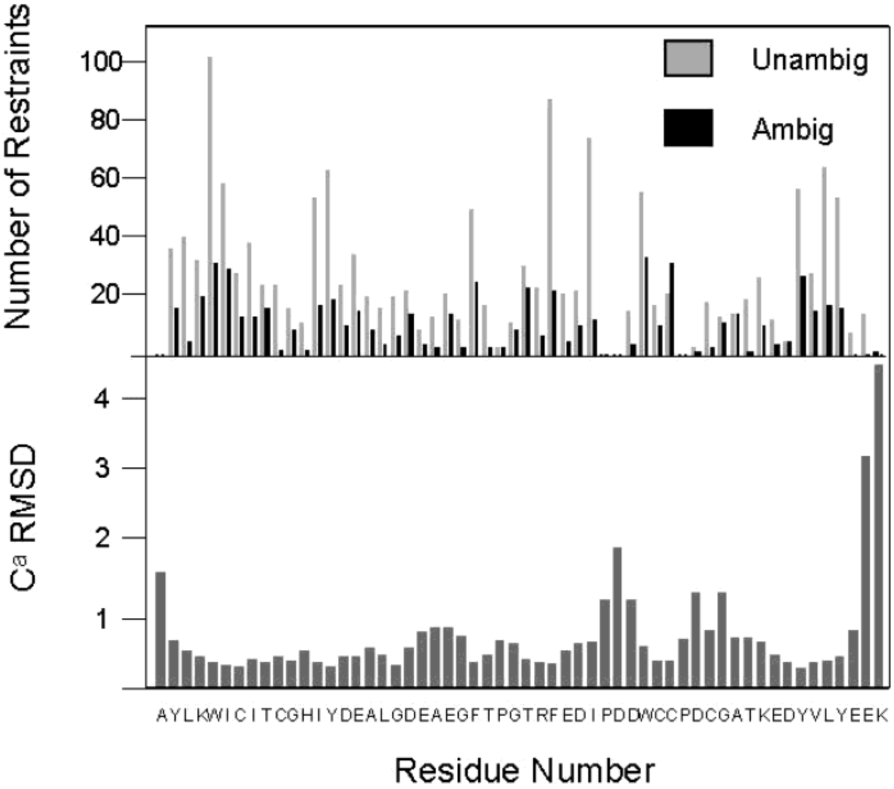

FIGURE 3: Plots of structural parameters. Upper panel, the distribution of unambiguous and ambiguous restraints. Lower panel, C^{α} RMSD relative to the mean coordinates calculated with XPLOR (*43*).

close proximity of molecules at high concentration) and aggregation, both of which are characterized by increases in intensity at low scattering angles. While any aggregation will be evident in both high and low concentration samples, any interparticle effects observed are reduced at low concentration. The profile obtained for the sample at 12.8 mg/mL and the corresponding intraparticle distance distribution function is shown in Figure 5A. Comparison of this scattering profile with the one obtained at a protein concentration of 1 mg/mL demonstrated the protein is monodispersed, with no protein aggregation or interparticle effects evident.

Multiple data sets allowed several shape calculations to be carried out; Figure 5B represents a typical shape for C-Rb. The theoretical scattering calculated from the restored shape is shown as a smooth profile in Figure 5A. All the calculations yielded very similar conformational characteristics, highlighting the consistency of the low resolution models. The low resolution molecular shape for C-Rb is a globular, compact domain with an extended “tail” (Figure 5B). The domain envelope calculated here can effectively accommodate the dimensions of the C-terminal “core” domain obtained from the high-resolution NMR structure. Thus, the structural arrangement comprising a compact domain plus extended tail concurs with the overall structure obtained by NMR. When numerous shape restoration runs were performed the highly flexible nature of the linker in C-Rb was characterized by significant conformational variability compared with the folded domain. However, the flexibility of the linker is reduced in the vicinity of the peptide segment where it is anchored to the core domain. Consequently, only about half of the ∼30-amino acid residue linker is poorly structured.

Solution X-ray Scattering of AlkG Containing One and Two Bound Irons. Scattering data analysis was performed on AlkG bound to either one (C-terminal domain) or two (C- and N-terminal domains) iron atoms. These proteins were expressed and purified as described by Lee et al. (*23*). The protein containing two iron atoms was found to be inhomogeneous, resulting in poor fits between the experimental data and the reconstructed shape. This inhomogeniety was attributed to the presence of partially folded states produced following the harsh procedure (involving precipitation, unfolding, and resolubilization) that is necessary to incorporate the iron into the N-Rb domain of AlkG. This iron atom is lost during AlkG purification (*20*). No further analysis of X-ray scattering data obtained for AlkG bound to two iron atoms was carried out.

Scattering profiles for AlkG containing one iron atom in the C-Rb domain, i.e., the form purified from *Ps. oleovarans* or recombinant strains of *E. coli* (*23*), were collected at protein concentrations of 1 and 30 mg/mL. The composite profile obtained with high and low concentration samples, and the intraparticle distance distribution function, are shown in Figure 6A. The scattering profile shows that the protein is monodisperse, with no protein aggregation or interparticle effects. A composite of the data collected at high and low concentration was used for the molecular shape calculations. Figure 6B displays a typical shape profile reconstructed from the scattering curve shown in Figure 6A. The theoretical scattering curve from the restored shape is superimposed as a smooth line on the experimental data in Figure 6A. Good agreement between experimental and theoretical data is provided over the whole scattering range, which indicates that even contributions from inhomogeneities at higher scattering angles due to this flexible

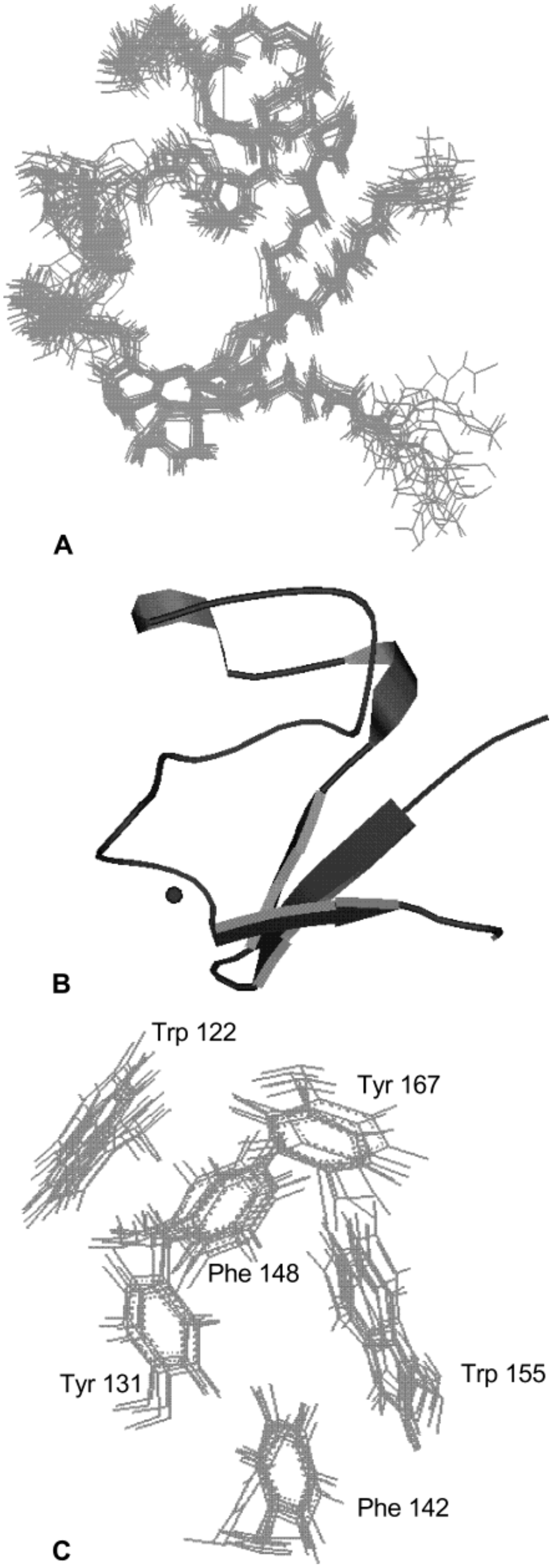

FIGURE 4: (A) The ensemble of 20 NMR structures for the C-Rb domain. Taken from the 20 lowest energy structures from the final iteration. (B) A ribbon representation of the C-Rb domain in the same orientation as panel A. (C) Relative orientations of the hydrophobic residues of the 20 lowest energy NMR structures. Residues include the six aromatic residues Trp 122, Tyr 131, Phe 142, Phe 148, Trp 122, Tyr 166, and Trp 155 and the hydrophobic side-chain Ile 151.

Table 1: Structural Statistics[a]

restraints for structure calculation	
total restraints	900
total NOE restraints	878
intraresidue	358
sequential	185
medium range ($2 < \|i - j\| < 4$)	94
long-range ($\|i - j\| \geq 5$)	241
H-bond restraints	14
cadmium distance restraints	8
atomic rmsd	
backbone atoms (Å)	0.71 ± 0.1 (for the NMR ensemble)
all heavy atoms (Å)	1.29 ± 0.1 (for the NMR ensemble)
procheck analysis	
most favored regions	73.6%
additionally allowed	22.7%
generously allowed	3.5%
disallowed	0.2%

[a] The average energies for the 20 structures of the NMR ensemble.

Table 2: Backbone RMSD Values of Rubredoxins vs C-Rb[a]

organism	PDB ID code	RMSD vs C-Rb[a]
Clostridium pasteurianum	5rxn	1.04
Desulfovibrio gigas	1rdg	1.21
Desulfovibrio vulgaris	7rxn	1.04
Pyrococcus furiosus	1brf	1.03

[a] All residue backbone RMSD values were calculated using MODELLER-4. The lowest energy structure from the NMR ensemble was used for the C-Rb structure.

and low molecular weight protein are appropriately taken into account.

The molecular model for AlkG containing iron in the C-Rb domain can be characterized by two globular domains connected by a linker peptide region (Figure 6B). The linker region in AlkG is not completely mobile/extended and therefore does not confer motional independence between the folded N- and C-terminal rubredoxin domains. The AlkG linker places the two rubredoxin domains in close proximity. Earlier NMR studies of AlkG had also suggested interactions between the N- and C-terminal domains (*23*), and this is consistent with our data from X-ray scattering studies. Because of the resolution limit inherent in shapes reconstructed from X-ray solution scattering data, the fitting of a compact high-resolution atomic structure into a compact shape model consisting of spheres representing amino acids is not clear-cut, i.e., it is easy to fit the model in a wrong orientation. This is indicated by the results using the program SUPCOMB (*35*) which provided several possible solutions with very similar goodness-of-fit values. Thus, we have to note that the orientations of the redox centers in Figure 7B was not driven by the shape fitting but rather favored by the shortest possible distance between the Fe-atoms, which will favor interdomain electron transfer.

Interaction of AlkG and Its Domains with Rubredoxin Reductase. Our previous studies have indicated that N-Rb prepared by Factor-Xa cleavage of the AlkG-His protein has a half-life of ∼3.5 h when prepared in buffers lacking glycerol (*20*). This is a significant improvement in terms of the poor stability of the N-terminal domain (half-life ∼ 30 min) released by cyanogen bromide treatment of AlkG (*25*),

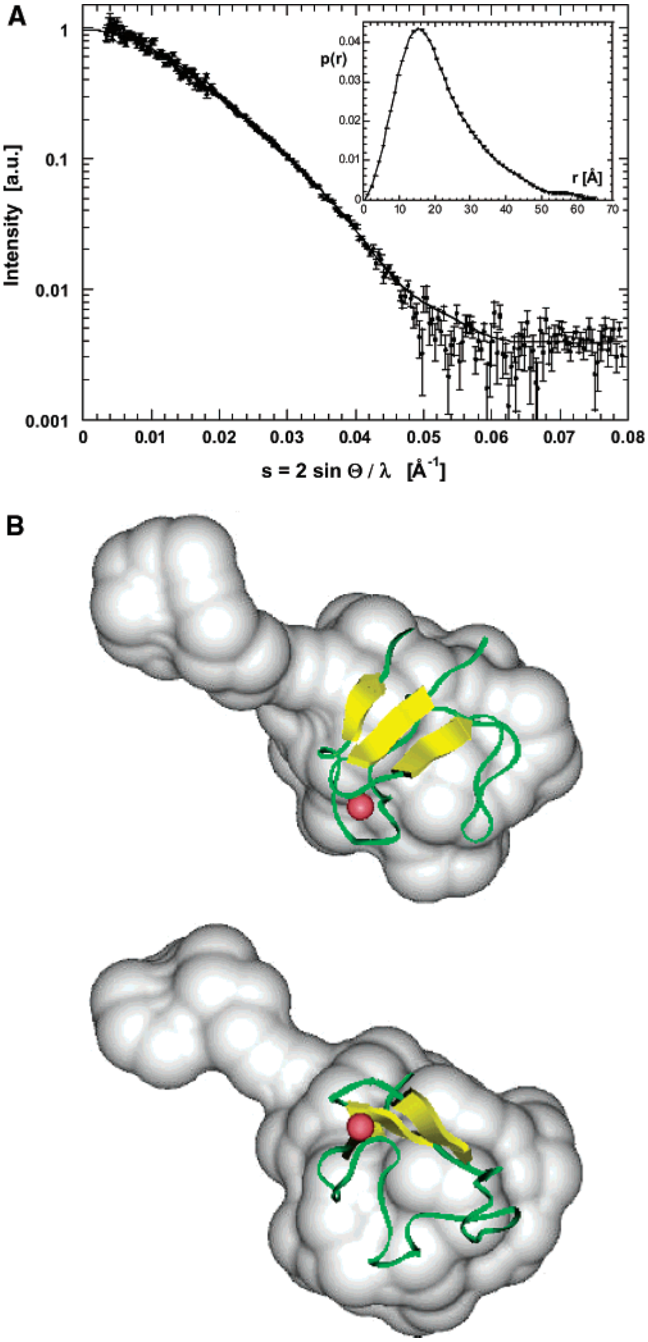

FIGURE 5: (A) Solution X-ray scattering profile (main panel) and *p*(*r*) function (inset) for the C-Rb domain. The experimental scattering curve is the result of merging the data for low (1 mg/mL) and high (12.8 mg/mL) protein concentrations. The calculated structural parameters are R_g = 16.9 Å, D_{max} = 64 Å, and V = 18000 Å^3. The smooth curve in the main panel represents the scattering profile from the restored shape displayed in panel B. (B) Two orthogonal orientations of the low resolution shape model for the C-Rb domain calculated from the X-ray scattering data shown in panel A. The superimposed backbone ribbon is taken from the NMR structure of C-Rb. The graphics in panel B were produced with Insight II (Biosym/MSI).

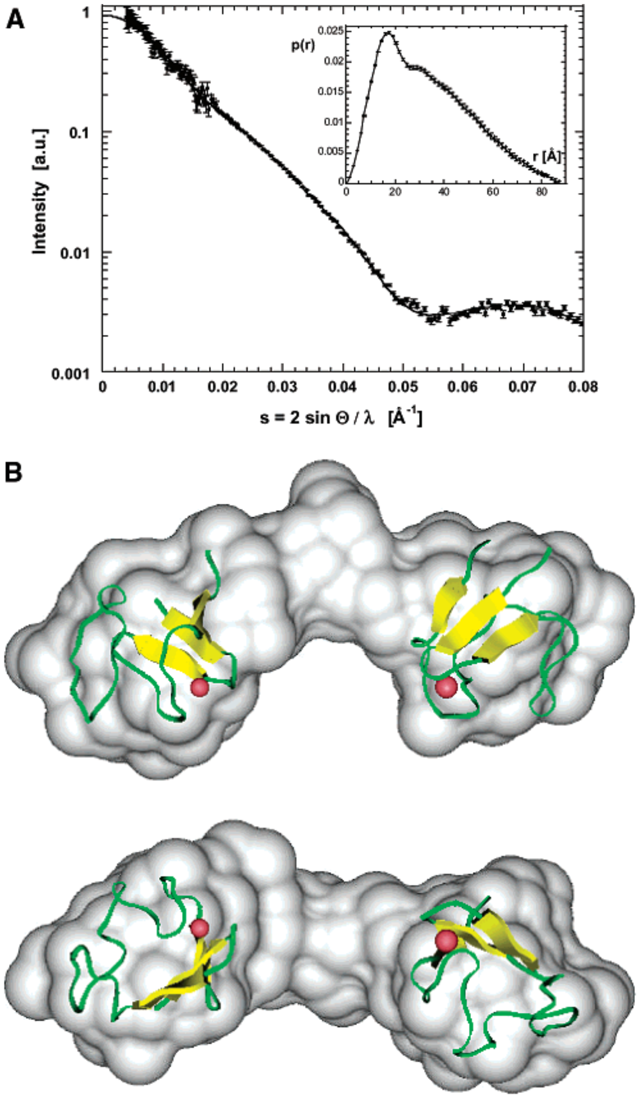

FIGURE 6: (A) X-ray scattering profile (main panel) and *p*(*r*) function (inset) for Alk G as purified (i.e., with iron bound only to the C-Rb domain). Scattering data has been merged for low (1 mg/mL) and high (30 mg/mL) concentration. Samples were contained in 20 mM potassium phosphate buffer, pH 7.6. The calculated structural parameters are R_g = 26.3 Å, D_{max} = 87 Å and V = 36000 Å^3. (B) Two orientations of the low resolution structure for AlkG calculated from the X-ray scattering data shown in panel A. The superimposed backbone ribbons are taken from the NMR structure of C-Rb and a modeled structure of N-Rb. The graphics in panel B were produced with Insight II (Biosym/MSI).

which probably reflects the location of the unique methionine residue close to the domain boundary of the N-terminal domain (*40*). The enhanced stability of the Factor Xa cleaved N-Rb is most likely attributable to preservation of domain structure following cleavage since the protease recognition site is located at a central point in a large (~70-amino acid residue) linker that separates the N-Rb and C-Rb domains (*20*). Even so, the relatively short half-life (~3.5 h) of the isolated N-Rb domain following reconstitution with iron compromises biophysical studies of electron-transfer complex assembly. Thus, for functional studies of the interaction of N-Rb and C-Rb domains with RR we sought ways of stabilizing the N-Rb domain through the inclusion of glycerol in the refolding buffer. In the absence of glycerol, N-Rb is substantially less stable than C-Rb, 1Fe-Rb, and 2Fe-Rb, but inclusion of glycerol increases the stability of N-Rb [half-life increased from 3.5 (no glycerol) to 17 h (20% v/v glycerol); see Supporting Information]. Over a 24 h period and in the absence of glycerol, C-Rb and 1Fe-Rb do not lose absorption in the visible region and extended incubations (98 h) indicated these proteins are very stable. Visible absorption is lost for 2Fe-Rb over a 24 h period, indicating

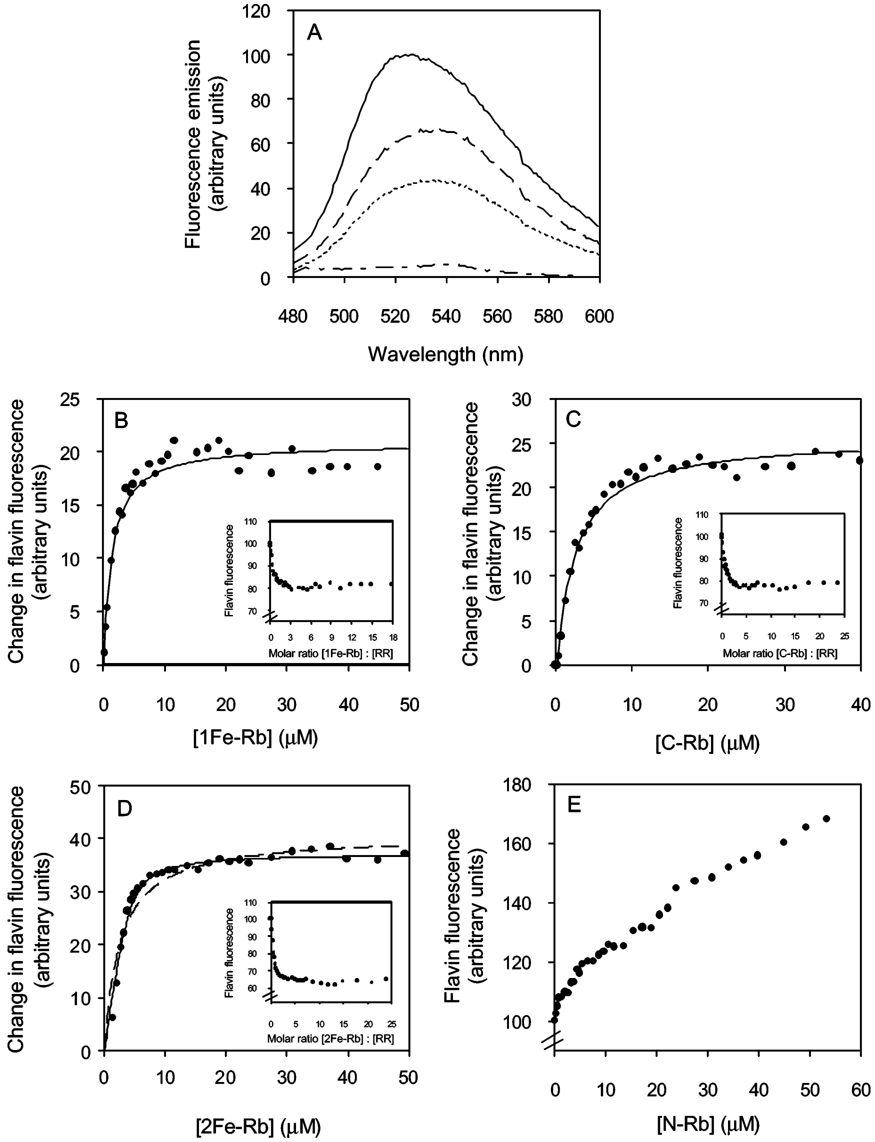

FIGURE 7: Equilibrium binding studies of RR to the rubredoxin and the N-Rb and C-Rb domains. (A) Quenching of FAD fluorescence at 530 nm. Spectra (upper to lower respectively) are as follows: emission spectrum for RR (4 μM); emission spectrum for RR (4 μM) in the presence of 1Fe-Rb (120 μM) after correction for inner filter effects; emission spectrum for RR (4 μM) in the presence of 2Fe-Rb (120 μM) after correction for inner filter effects; baseline emission recorded for a solution of 2Fe-Rb alone (120 μM). The peak emission value of RR at 530 nm was arbitrarily set as 100. (B) Binding curve for the interaction of RR with 1Fe-Rb. Inset, plot of flavin fluorescence against molar ratio of 1Fe-Rb:RR. (C) As for panel B, but for interactions with C-Rb. (D) As for panel B, but for interactions with 2Fe-Rb. Solid line, fit to data using a quadratic function (eq 1); dashed line, fit to data using a hyperbolic function. (E) change in flavin fluorescence as a result of N-Rb-induced FAD release from RR. Conditions: 100 mM Tris-HCl buffer, pH 7.3; 22 °C.

loss of iron from the N-terminal domain. The stability of 2Fe-Rb is enhanced by glycerol, but the effect is small suggesting that the N-terminal domain is partially stabilized by the presence of the C-terminal domain. Consistent with this view, the NMR and small-angle X-ray scattering studies of 1Fe-Rb indicate close juxtaposition of the two domains, and this close association might confer stability on N-Rb.

The use of glycerol to stabilize the activity of RR has been documented in earlier work (*9*, *24*), but detailed analysis of the stabilizing effects have not been reported. We exploited the low intrinsic fluorescence properties of the FAD in RR in stability assays, since release of FAD from RR leads to an increase in FAD fluorescence emission. The inclusion of glycerol (20% v/v) prevents FAD loss from RR over a 24-h period (data shown in Supporting Information). In the absence of glycerol, the increase in FAD fluorescence parallels the loss of enzyme activity. Addition of various rubredoxin proteins was found to be effective in preventing the loss of FAD from RR, even in the absence of glycerol. Among the rubredoxins, C-Rb is the most effective in preventing loss of FAD from RR in the absence of glycerol, and N-Rb is the least effective (even in the presence of 20% v/v glycerol). A 10-fold molar excess of C-Rb stabilizes RR fully over the 24 h period, but a 30-fold molar excess of 1Fe-Rb and 2Fe-Rb is required to afford the same protection against loss of FAD. N-Rb actually destabilizes RR even in the presence of 20% (v/v) glycerol, which suggests a different mode of binding to RR compared to C-Rb. However, the N-Rb domain does not destabilize RR when present in full-length rubredoxins (i.e., 1Fe-Rb and 2Fe-Rb).

Quantitative analysis of the binding of C-Rb, N-Rb, 1Fe-Rb, and 2Fe-Rb to RR was performed by monitoring the quenching of FAD fluorescence on complex formation

Table 3: Dissociation Constants for the RR−Rubredoxin Complexes Determined from Quantitative Analysis of Fluorescence Binding Data Using Eq 1

rubredoxin	concentration of KCl in buffer (M)	K_d (μM)
2Fe-Rb	0	0.6 ± 0.1
C-Rb	0	1.7 ± 0.2
1Fe-Rb	0	1.1 ± 0.1
1Fe-Rb	0.2	1.2 ± 0.1
1Fe−Rb	0.4	1.2 ± 0.1
1Fe−Rb	0.6	1.8 ± 0.2
1Fe−Rb	0.8	1.2 ± 0.1
1Fe−Rb	1.0	1.3 ± 0.2

with RR (Figure 7). The quenching of FAD fluorescence upon binding of rubredoxin (120 μM) to RR (4 μM) is shown in Figure 7A. Rubredoxin does not emit fluorescence at 530 nm when excited at 458 nm, but at 120 μM it accounts for ∼35% quenching of free FAD fluorescence through the inner filter effect. Inner filter effects were determined for each form of rubredoxin, and the inner filter and dilution effects were accounted for in the analysis of binding titrations with RR (Figure 7, panels B−E). Dissociation constants for protein complexes (Table 3) were determined by quantitative analysis of binding data using eq 1. 1Fe-Rb and C-Rb bind to RR with similar affinities, and the maximum degree of quenching of FAD fluorescence was similar for all these proteins. The dissociation constant for the complex formed between RR and 2Fe-Rb is about 2−3-fold smaller than with 1Fe-Rb and C-Rb, perhaps suggesting some additional interaction between the iron-containing N-Rb domain of 2Fe-Rb and RR. The higher affinity of the 2Fe-Rb for RR is apparent in Figure 7D, where the deviation from a hyperbolic binding equation (dashed line) is more apparent than with the C-Rb and 1Fe-Rb proteins. Binding assays performed at high ionic strength did not significantly affect the dissociation constant for 1Fe-Rb (Table 3) or 2Fe-Rb and C-Rb (data not shown). The addition of N-Rb to RR did not elicit any quenching of FAD fluorescence after correction for the inner filter effect. Rather, the flavin fluorescence emission increased with increasing N-Rb concentration (Figure 7E), consistent with the known destabilizing effect of N-Rb on RR stability (see above).

The kinetics of complex assembly were investigated by rapid mixing stopped-flow methods using the fluorescence of FAD in RR to monitor the binding reaction. Over short time bases (i.e., 60 ms), time-dependent quenching of FAD fluorescence was not observed on the binding of 1Fe-Rb, 2Fe-Rb, and C-Rb (each 40 μM) to RR (4 μM; e.g., see Figure 8B). However, the fluorescence intensity is less than that observed for the rapid mixing of RR with buffer, indicating that some quenching of FAD fluorescence occurs in the dead time (1 ms) of the stopped-flow instrument. Similar observations were made when reactions were performed with 1Fe-Rb, 2Fe-Rb, and C-Rb at lower concentrations (8−40 μM, i.e., in the non-pseudo-first-order regime); under these conditions the extent of quenching that occurred in the dead time of the stopped-flow instrument progressively diminished as the concentration of rubredoxin was decreased. From knowledge of the K_d values for complex formation (Table 3), at equilibrium one expects 3.9 μM complex to form for the transient shown in Figure 8B, and from equilibrium binding measurements the expected fluorescence quench is around 10% of the initial fluorescence value. However, in the stopped-flow transient, the observed fluorescence quench is much less than that expected from the equilibrium binding measurements described above. This prompted further investigation using stopped-flow methods over an extended time domain (100 s at 25 °C) to assess if equilibrium had been attained. Fluorescence transients indicated substantial quenching of emission over this extended time domain for reactions with 2Fe-Rb, 1Fe-Rb, and C-Rb (Figure 8C). Rate constants were determined by approximating these large fluorescence changes to a monophasic kinetic process. These rate constants were found to be independent of rubredoxin concentration (4−100 μM). The data indicate that complex assembly is a multistep reaction involving rapid initial binding (small quenching of fluorescence in the dead time of the stopped-flow instrument) followed by a much slower conformational adjustment of the complex that gives rise to a substantial quenching of FAD fluorescence. The time scale for the slow conformational readjustment of the complex seen in stopped-flow experiments is consistent with the equilibration time (∼60 s; see above) required in static binding experiments to observe stable fluorescence emission. Stopped-flow studies over a short time period (60 ms) in which N-Rb (80 μM) was rapidly mixed with RR (4 μM) did not elicit a quenching of FAD fluorescence in the dead time of the instrument. Over an extended time period (100 s), a gradual increase in FAD fluorescence was observed (see Supporting Information), consistent with observations made in the equilibrium titration experiments with N-Rb. This increase in fluorescence emission is attributed to the N-Rb-induced loss of FAD from RR.

Electron-Transfer Studies. It has been reported previously that AlkG is required to mediate electron transfer from RR to cytochrome *c*, and that the reduction of cytochrome *c* is a convenient assay for determining RR activity (*24*). Similar assays have also been used to demonstrate that C-Rb and N-Rb can also mediate electron transfer from RR to cytochrome *c* (*20*), although in both cases measured rates had not taken into account the fact that cytochrome *c* can be directly reduced (albeit it slower rates) by RR in the absence of rubredoxin. Our studies described in this paper revealed that RR is able to transfer electrons from NADH to cytochrome *c* even in the absence of AlkG or its domains (Figure 9A). The exclusion of glycerol in previously published steady-state assays probably accounts for the lack of observable cytochrome *c* reductase activity in the absence of AlkG. This follows because glycerol is required to stabilize RR when AlkG is not present (see above). In the presence of AlkG the reduction of cytochrome *c* is more rapid than in its absence (Figure 9B), thus demonstrating that AlkG mediates electron transfer from RR to cytochrome *c*. Steady-state kinetic parameters for the reduction of cytochrome *c* mediated by the different rubredoxins (Table 4) indicate that the turnover number with N-Rb is ∼6-fold less than that for C-Rb and 1Fe-Rb. That N-Rb is a poor mediator is also evident from the fact that the turnover number is only 2-fold greater than the turnover value measured in the absence of any rubredoxin.

The multicomponent coupled assay described above provides limited insight into the ability of RR to transfer electrons to the different forms of rubredoxin since the

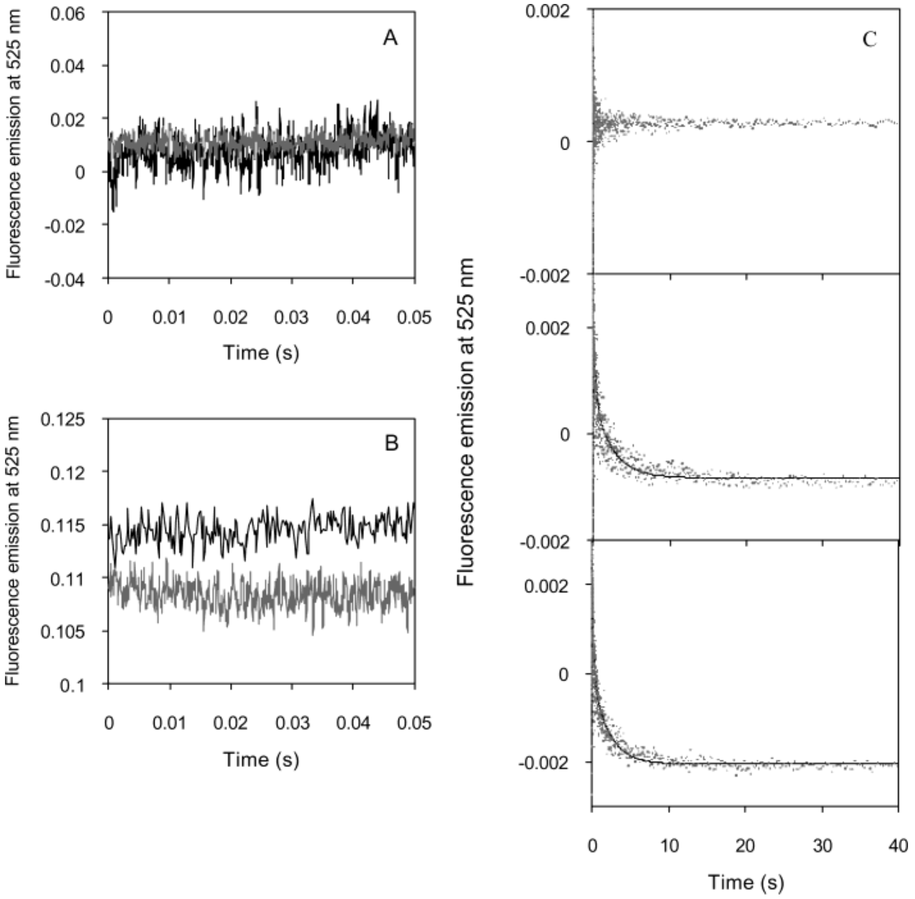

FIGURE 8: Short time base stopped-flow fluorescence transients for electron-transfer complex formation between RR and 1Fe-Rb. (A) Transients for the mixing of RR (4 μM) with buffer (gray trace) and RR (4 μM) with 1Fe-Rb (8 μM; black trace). (B) Transients for the mixing of RR (4 μM) with buffer (gray trace) and RR (4 μM) with 1Fe-Rb (40 μM; black trace). Conditions: 100 mM Tris-HCl buffer, pH 7.3, glycerol (20% v/v); 5 °C. Excitation 458 nm; fluorescence emission monitored using an edge pass filter (525 nm). (C) Long time base stopped-flow fluorescence transients for electron-transfer complex formation between RR and 1Fe-Rb or C-Rb. Conditions as for panels A and B except at 25 °C. Upper panel. Transient obtained on mixing RR (4 μM) with buffer. Central panel. Transient obtained on mixing RR (4 μM) with 1Fe-Rb (40 μM). Lower panel. Transient obtained on mixing RR (4 μM) with C-Rb (40 μM).

contribution of individual rate constants to the turnover number is not known. We have therefore performed stopped-flow studies of electron transfer from RR to C-Rb and N-Rb using sequential stopped-flow methods developed previously for studying electron transfer to 1Fe-Rb and 2Fe-Rb (*9*). As with our previous studies with 1Fe-Rb and 2Fe-Rb (*9*), an aging time of 5 s was employed to allow complete reduction of RR with NADH (*9*) prior to the second mix with C-Rb or N-Rb. With C-Rb, the observed rate constant for electron transfer displayed a hyperbolic dependence on C-Rb concentration (Figure 9C). The limiting rate of electron transfer (61.2 ± 1.4 s^{-1}) and apparent dissociation constant (12.7 ± 1.1 μM) for the complex were calculated by fitting to a standard hyperbolic expression:

$$k_{\mathrm{obs}} = \frac{k_{\mathrm{lim}}[R]}{K + [R]} \tag{2}$$

where k_{lim} is the limiting rate of electron transfer and K is the rubredoxin concentration at which half the limiting rate of electron transfer is achieved. The kinetic parameters are similar to those calculated previously for reactions with 1Fe-Rb and 2Fe-Rb (Table 4). With N-Rb, observed reaction rates showed a linear dependence on N-Rb concentration, indicating a very high dissociation constant for the complex (Figure 9D). These data indicate that N-Rb interacts differently with RR compared to C-Rb, 1Fe-Rb, and 2Fe-Rb, but is able to accept electrons from RR. The availability of the individual rubredoxin domains presented an opportunity to also investigate the rates of electron transfer between the domains. Our previous kinetic studies suggested that interdomain electron transfer within 2Fe-Rb is rapid [the minimum value for the rate constant for interdomain electron transfer in 2Fe-Rb is greater than the limiting rate for interprotein electron transfer between RR and 2Fe-Rb (i.e., >55 s^{-1}; Table 4)], owing to the lack of observable intermediates in the transfer of two electrons from RR to 2Fe-Rb (*9*). Fast electron transfer between the domains presumably arises owing to the tethering in close proximity of the C-Rb and N-Rb domains. Initial studies were aimed at identifying a suitable wavelength for monitoring interdomain electron transfer. C-Rb was titrated against dithionite and then mixed with oxidized N-Rb in a Yankeelov cell (i.e., dual chamber optical cuvette) under anaerobic conditions. The difference spectrum on mixing the two solutions indicates an increase in absorbance in the visible region (Figure 10A). Similarly, a decrease in absorbance in the visible region occurs on mixing dithionite-reduced N-Rb with oxidized C-Rb (Figure 10B). These spectral changes indicate that electrons are transferred reversibly between the individual domains. This is consistent

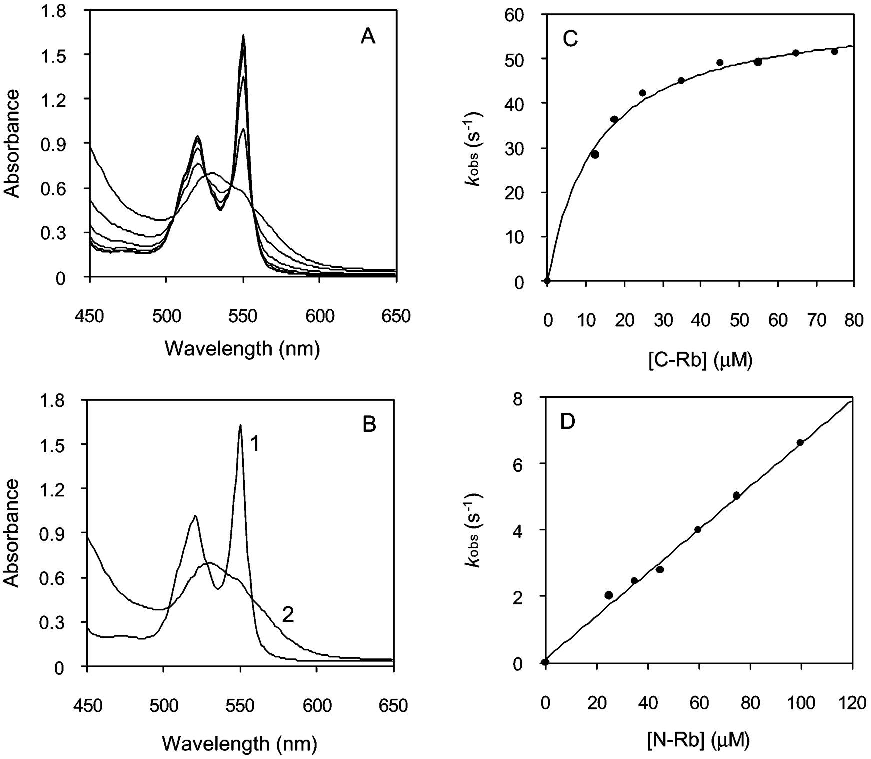

FIGURE 9: Kinetics of electron transfer in steady-state and stopped-flow studies. (A) Spectral changes accompanying the reduction of cytochrome *c* by RR in the absence of added rubredoxin. Conditions: 100 mM Tris-HCl buffer, pH 7.3, glycerol (20% v/v), 30 °C. Spectra shown in order of decreasing absorbance at 550 nm were taken at 0.5, 1, 1.5, 2 and 5 min, respectively. (B) As for panel A, but including 1Fe-Rb (2 μM). The final spectrum for reduced cytochrome *c* was obtained within the manual mixing time (i.e., <20 s). In panels A and B, cytochrome *c*, RR and NADH concentrations were 83, 2, and 300 μM, respectively. (C, D) Plots of observed rate constant for reduction of rubredoxin by NADH-reduced RR against rubredoxin concentration. (C) Data for the reaction of C-Rb with NADH-reduced RR. (D) As for panel C, but for reaction with N-Rb. For reaction conditions see Experimental Procedures. Kinetic constants derived from these plots are shown in Table 2.

Table 4: Steady-State Kinetic Parameters for the Rubredoxin-Mediated Reduction of Cytochrome *c* by RR and Stopped-Flow Kinetic Parameters for Electron Transfer from Reduced RR to the Different Rubredoxin Forms

	2Fe-Rb	1Fe-Rb	C-Rb	N-Rb
		Cytochrome c Coupled Assay Parameters		
k_{cat} (s^{-1})		0.61 ± 0.03	0.61 ± 0.03	0.11 ± 0.01
K_m (μM)		116 ± 12	81 ± 10	12 ± 1
k_{cat}/K_m (s^{-1}μM^{-1}) (× 10^3)		5.2 ± 0.8	7.5 ± 1.3	9.3 ± 1.6
		Stopped-Flow Parameters[a]		
k_{lim} (s^{-1})	55.2 ± 0.3	72.7 ± 0.6	61.2 ± 1.4	
K (μM)	4.5 ± 0.2	12.5 ± 0.5	12.7 ± 1.1	
k_{lim}/K (s^{-1}μM^{-1})	12.3 ± 0.6	5.8 ± 0.3	4.8 ± 0.5	0.065[b]

[a] Stopped-flow parameters for reactions with 2Fe-Rb and 1Fe-Rb are taken from ref *10*. [b] Calculated from the gradient of a plot of observed rate constant against N-Rb concentration (see Figure 9D).

with the known midpoint reduction potentials of both domains in 2Fe-Rb, which are essentially isopotential [∼ −6 mV; (*23*)]. Initial rates of interdomain electron transfer from N-Rb to C-Rb and vice versa were exceptionally slow and calculated from time-dependent absorption data measured at 510 nm in a conventional spectrophotometer under anaerobic conditions (Table 5). Initial rates were dependent on the concentration of the reacting components, suggesting a bimolecular process (Table 5). Complete equilibration of electrons occurred over an extended time period (>1000 s). We infer that the exceptionally slow rates reflect the very weak interaction of the two domains in the absence of covalent linkage. This is consistent with the structural model derived from NMR and small-angle X-ray scattering studies of AlkG, which suggest that domain−domain interaction is not extensive, and that the 70-amino acid linker is thus responsible for bringing the two redox domains together to facilitate rapid interdomain electron transfer in 2Fe-Rb.

DISCUSSION

Microbial genome sequencing projects have led to the identification of a number of rubredoxins that are likely to be involved in the oxyfunctionalization of alkanes (*41*). A number of these rubredoxins have been cloned from Gram-positive and Gram-negative organisms that are able to grow on alkanes, and in vivo complementation assays together with sequence comparison studies have indicated these can be divided into two groups, termed the AlkG1 and AlkG2-type rubredoxins (*41*). The AlkG1-type rubredoxins are more closely related to the N-terminal domain (N-Rb) of the *Ps. oleovorans* rubredoxin (AlkG); in contrast, the AlkG2-type rubredoxins are related more closely to the C-terminal domain (C-Rb). Only plasmids encoding the C-Rb domain of AlkG can restore growth on alkanes in strains lacking a functional rubredoxin, thus suggesting that the N-Rb domain is not essential for electron transfer between RR and alkane hydroxylase (*40*). More generally, the AlkG2-type rubredoxins from different microbial species, but not the AlkG1-type rubredoxins, are able to replace AlkG in complementation tests with recombinant strains of *E. coli* that contain all *Ps. oleovorans* genes necessary for growth on alkanes except for AlkG (*41*).

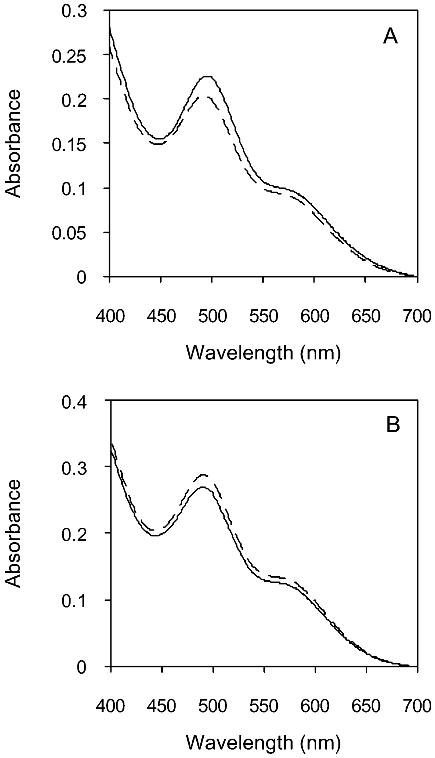

FIGURE 10: Spectral changes accompanying the mixing of reduced C-Rb with oxidized N-Rb (panel A) and oxidized C-Rb with reduced N-Rb (panel B). Conditions: 50 mM potassium phosphate buffer, pH 7.0, glycerol (20% v/v), 25 °C. Dashed line, spectrum before mixing; solid line, spectrum after mixing. In panel A, C-Rb and N-Rb concentrations are ~35 μM. In panel B, C-Rb and N-Rb concentrations are ~45 μM.

Table 5: Initial Rates of Interdomain Electron from C-Rb to N-Rb and vice versa[a]

Electron Transfer from Reduced N-Rb to Oxidized C-Rb

conc of N-Rb (μM)	conc of C-Rb (μM)	initial rate of electron transfer (ΔA_{500} min^{-1})
22	44	0.012
22	220	0.021

Electron Transfer from Reduced C-Rb to Oxidized N−Rb

conc of C-Rb(μM)	conc of N-Rb (μM)	initial rate of electron transfer (ΔA_{500} min^{-1})
20	40	0.003
20	200	0.008

[a] Reactions were performed at 25 °C, in 50 mM potassium phosphate buffer, pH 7.0, containing 20% glycerol. Complete equilibration of electrons occurred over an extended time period (>1000 s). Reaction progress was monitored at 500 nm.

To delineate more precisely the role of each domain of AlkG in electron transfer and binding, we have performed structural studies with AlkG and its component C-Rb domain and a series of interaction and kinetic studies using the isolated domains of AlkG (i.e., C-Rb and N-Rb). Biochemical studies have shown that the iron in the N-Rb domain is loosely bound and is lost on purification of AlkG from *Ps. oleovorans* or recombinant *E. coli* hosts (*25, 23*). Reconstitution of AlkG (the 1Fe-Rb form), however, is relatively facile and yields the 2Fe-Rb form of AlkG. The propensity of the N-Rb domain to lose iron (both in AlkG and the isolated N-Rb domain) is a major impediment in both structural studies of the isolated N-Rb domain and biophysical studies of domain function. However, we have shown that the inclusion of glycerol substantially increases the half-life of the N-Rb domain, thus facilitating functional characterization, although structural studies using NMR spectroscopy are still out of reach. Moreover, we have demonstrated that glycerol also protects against loss of FAD from RR and that the two forms of AlkG (2Fe-Rb and 1FeRb) and C-Rb also afford protection in the absence of glycerol. These data suggest that 2Fe-Rb, 1Fe-Rb, and C-Rb bind to RR close to the FAD, thus preventing loss of the cofactor. This is consistent with the quenching of FAD fluorescence in equilibrium binding studies of the electron-transfer complex formed between RR and 2Fe-Rb, 1FeRb, and C-Rb (Figure 7).

Our kinetic studies reveal that both N-Rb and C-Rb can mediate electron transfer from RR to cytochrome *c* (Table 4), although with N-Rb the enhancement in rate above that observed for direct reduction of cytochrome *c* in the absence of rubredoxin is small (~2-fold). The ability of N-Rb to accept electrons from RR was also demonstrated in stopped-flow studies (Table 4), but in this case N-Rb was shown to be a poor electron acceptor compared with 2Fe-Rb, 1Fe-Rb, and C-Rb. This suggests that the relatively small difference in reactivity measured in the cytochrome *c* reduction assays (i.e., N-Rb compared with C-Rb, and 1Fe-Rb) is attributed to poor rates of electron transfer to cytochrome *c*. The mode of interaction of N-Rb with RR is clearly different from the other rubredoxin forms. This is apparent from the lack of saturation in studies of the observed electron-transfer rate versus N-Rb concentration in stopped-flow kinetic studies (Figure 9) and also from equilibrium and stopped-flow binding studies that reveal no quenching of FAD fluorescence. Indeed, association with N-Rb appears to destabilize (rather than stabilize as seen with C-Rb, AlkG) RR, as inferred from the increase in FAD fluorescence emission. Combined with the evidence gained from in vivo complementation assays (*40, 41*), our data point toward the C-Rb domain of AlkG being the immediate electron acceptor from RR. Moreover, we have shown that electron transfer likely occurs in a metastable form of the electron-transfer complex, although it is acknowledged that the long time base fluorescence changes observed on mixing RR with C-Rb, 1Fe-Rb, and 2Fe-Rb are for the oxidized proteins and not the competent electron-transfer complex. The precise role of the N-Rb domain in its association with RR remains unclear except that in vivo AlkG (in the 2Fe-Rb form) has a two-electron capacity and can therefore mediate two-electron transfer to membrane-bound hydroxylase, as demanded by the hydroxylation chemistry. This is clearly desirable compared with the alternative mechanism involving the sequential formation of two RR-AlkG (1Fe-Rb) complexes. In the latter case, each complex only has the capacity to transfer a single electron. There is a requirement for relatively rapid electron transfer from the C-Rb to N-Rb domain in an electron-transfer mechanism that involves the formation of a single complex between RR and AlkG (2Fe-Rb). This follows since reoxidation of the C-Rb domain by electron transfer to N-Rb is required prior to transfer of the second electron from RR to C-Rb; these electron movements must occur before the complex dissociates. In the absence of the 70-amino acid linker, the rates of interdomain electron transfer are very slow. We infer, therefore, that the linker is required to position in relatively close proximity the two redox domains of AlkG (in the AlkG-RR complex) to facilitate interdomain electron transfer. The X-ray scattering analysis of free AlkG with iron bound only to the C-Rb domain is consistent with a structure comprising two folded domains in relative close proximity, although these domains might need to be more closely juxtaposed in the RR-AlkG complex to enable rapid electron transfer. Although the iron atoms in the C-Rb and N-Rb domains are approximately 30 Å apart in the model shown in Figure 6B, it is conceivable that the linker segment will allow movement so as to reduce this Fe−Fe separation to 10−20 Å. This shorter distance is within acceptable distances for electron-transfer based on structural analyses of many redox proteins (*42*). Further structural studies of the complex are needed to establish any relative domain movement on binding to RR. That said, the structural model derived from small-angle X-ray scattering studies suggests some restriction in flexibility in the linker region perhaps suggesting the absence of major domain motion in the electron-transfer complex. The limited NMR studies performed on AlkG also concur with these findings (*23*). The surface of C-Rb did not reveal obvious regions of charge build-up or large hydrophobic patches, which is consistent with the lack of ionic strength effects on the interaction of C-Rb with RR.

Sequence differences between the N-Rb and C-Rb domains have been explored in an attempt to identify structural changes that allow productive association with RR and/or alkane hydroxylase (*41*). Each domain has two iron-binding motifs (CXXCG), and most rubredoxins involved in alkane hydroxylation possess four negatively charged residues that are not conserved in other rubredoxins. In N-Rb and C-Rb, the location of these residues has been modeled on the basis of the *P. furiosus* rubredoxin (*41*), and their modeled location is consistent with the NMR structure of C-Rb. Two of the acidic residues are located on opposite sides of the redox center, while the two other acidic residues are further away from the iron. These residues are conserved in N-Rb and C-Rb, suggesting they are not important in domain recognition by RR, which is also consistent with the lack of an ionic strength dependence on formation of the protein complex between RR and C-Rb or AlkG (Table 3). A key difference between the N-Rb and C-Rb domains, however, is the presence of an arginine residue downstream of the second CXXCG motif in the N-Rb domain which is absent in the C-Rb domain. Mutagenesis studies have indicated that the presence of this arginine residue prevents transfer of electrons to alkane hydroxylase in growth assays (*41*). It has been suggested that this arginine residue in the N-Rb domain might sterically prevent association of the N-Rb domain with RR in a conformation that is compatible with formation of a productive electron-transfer complex.

In summary, taken with data published previously on the full-length AlkG proteins (*9*), our studies have indicated that the C-Rb domain is the primary acceptor of electrons from RR in the RR−AlkG complex. In vivo, we suggest the N-Rb domain does not receive electrons directly from RR, but becomes reduced following rapid electron transfer from the C-Rb domain. Electron transfer likely occurs in a metastable form of the RR−AlkG complex, since the most thermodynamically stable form of the complex forms only after extended time periods in rapid mixing stopped-flow experiments. C-Rb and AlkG stabilize the loss of FAD from RR and quench the emission of FAD fluorescence, suggesting close approach of rubredoxin to the cofactor in the electron-transfer complex. N-Rb is capable of accepting electrons from RR, but the slow rates of electron transfer and the inability of N-Rb to quench the emission of FAD fluorescence suggest this is a non physiological interaction. Work is in progress to ascertain whether it is the N-Rb and/or C-Rb domains that donate electrons directly to the membrane-bound alkane hydroxylase. On the longer term, the availability of the C-Rb domain of AlkG and the biochemical data for complex assembly should facilitate structural studies of the electron-transfer complex formed between RR and AlkG.

ACKNOWLEDGMENT

We thank Dr. J. Basran for assistance with preparation of some of the figures and for comments on the manuscript.

SUPPORTING INFORMATION AVAILABLE

COSY and NOESY spectra and a listing of ^{1}H HMR chemical shifts of Cd-substituted C-Rb at 25 °C and pH 6.0; data for stability studies of different rubredoxin forms and rubredoxin reductase; and stopped-flow fluorescence transients for the mixing of RR with N-Rb. This material is available free of charge via the Internet at http://pubs.acs.org.

REFERENCES

1. Sieker, L. C., Stenkamp, R. E., and LeGall, J. (1994) Rubredoxin in crystalline state. *Methods Enzymol. 243*, 203−216.
2. Jenney, F. E., Jr., Verhagen, M. F., Cui, X., and Adams, M. W. (1999) Anaerobic microbes: oxygen detoxification without superoxide dismutase. *Science 286*, 306−309.
3. Gomes, C. M., Silva, G., Oliveira, S., LeGall, J., Liu, M. Y., Xavier, A. V., Rodrigues-Pousada, C., and Teixeira, M. (1997) Studies on the redox centers of the terminal oxidase from *Desulfovibrio gigas* and evidence for its interaction with rubredoxin. *J. Biol. Chem. 272*, 22502−22508.
4. Chen, J. C., and Mortenson, L. E. (1992) Identification of six open reading frames from a region of the *Azotobacter vinelandii* genome likely involved in dihydrogen metabolism. *Biochim. Biophys. Acta 1131*, 199−202.
5. Wastl, J., Sticht, H., Maier, U. G., Rosch, P., and Hoffmann, S. (2000) Identification and characterization of a eukaryotically encoded rubredoxin in a cryptomonad alga. *FEBS Lett. 471*, 191−196.
6. Wastl, J., Duin, E. C., Iuzzolino, L., Dorner, W., Link, T., Hoffmann, S., Sticht, H., Dau, H., Lingelbach, K., and Maier, U. G. (2000) Eukaryotically encoded and chloroplast-located rubredoxin is associated with photosystem II. *J. Biol. Chem. 275*, 30058−30063.
7. Geissdorfer, W., Frosch, S. C., Haspel, G., Ehrt, S., and Hillen, W. (1995) Two genes encoding proteins with similarities to rubredoxin and rubredoxin reductase are required for conversion of dodecane to lauric acid in *Acinetobacter calcoaceticus* ADP1. *Microbiology 141*, 1425−1432.
8. Peterson, J. A., and Coon, M. J. (1968) Enzymatic omega-oxidation. 3. Purification and properties of rubredoxin, a component of the omega-hydroxylation system of *Pseudomonas oleovorans*. *J. Biol. Chem. 243*, 329−334.
9. Lee, H. J., Basran, J., and Scrutton, N. S. (1998) Electron transfer from flavin to iron in the *Pseudomonas oleovorans* rubredoxin reductase-rubredoxin electron-transfer complex. *Biochemistry 37*, 15513−15522.
10. Eggink, G., Engel, H., Vriend, G., Terpstra, P., and Witholt, B. (1990) Rubredoxin reductase of *Pseudomonas oleovorans*. Structural relationship to other flavoprotein oxidoreductases based on one NAD and two FAD fingerprints. *J. Mol. Biol. 212*, 135−142.
11. Eggink, G., van Lelyveld, P. H., Arnberg, A., Arfman, N., Witteveen, C., and Witholt, B. (1987) Structure of the *Pseudomo-*

nas putida alkBAC operon. Identification of transcription and translation products. *J. Biol. Chem. 262*, 6400−6406.

12. Bertini, I., Kurtz, D., Eidsness, M., Liu, G., Luchinat, C., Rosato, A., and Scott, R. (1998) Solution structure of reduced *Clostridium pasteurianum* rubredoxin. *J. Biol. Inorg. Chem. 3*, 401−410.
13. Blake, P. R., Park, J. B., Zhou, Z. H., Hare, D. R., Adams, M. W., and Summers, M. F. (1992) Quantitative measurement of small through-hydrogen-bond and "through-space" ^{1}H-^{113}Cd and ^{1}H-^{199}Hg J couplings in metal-substituted rubredoxin from *Pyrococcus furiosus. Protein Sci. 1*, 1508−1521.
14. Stenkamp, R. E., Sieker, L. C., and Jensen, L. H. (1990) The structure of rubredoxin from *Desulfovibrio desulfuricans* strain 27774 at 1.5 Å resolution. *Proteins 8*, 352−364.
15. Frey, M., Sieker, L., Payan, F., Haser, R., Bruschi, M., Pepe, G., and LeGall, J. (1987) Rubredoxin from *Desulfovibrio gigas*. A molecular model of the oxidized form at 1.4 Å resolution. *J. Mol. Biol. 197*, 525−541.
16. Adman, E. T., Sieker, L. C., and Jensen, L. H. (1991) Structure of rubredoxin from *Desulfovibrio vulgaris* at 1.5 Å resolution. *J. Mol. Biol. 217*, 337−352.
17. Dauter, Z., Wilson, K. S., Sieker, L. C., Moulis, J. M., and Meyer, J. (1996) Zinc- and iron-rubredoxins from *Clostridium pasteurianum* at atomic resolution: a high-precision model of a ZnS_4 coordination unit in a protein. *Proc. Natl. Acad. Sci. U.S.A. 93*, 8836−8840.
18. Day, M. W., Hsu, B. T., Joshua-Tor, L., Park, J. B., Zhou, Z. H., Adams, M. W., and Rees, D. C. (1992) X-ray crystal structures of the oxidized and reduced forms of the rubredoxin from the marine hyperthermophilic archaebacterium *Pyrococcus furiosus*. *Protein Sci. 1*, 1494−1507.
19. Lode, E. T., and Coon, M. J. (1971) Enzymatic omega-oxidation. V. Forms of *Pseudomonas oleovorans* rubredoxin containing one or two iron atoms: structure and function in omega-hydroxylation. *J. Biol. Chem. 246*, 791−802.
20. Perry, A., Lian, L. Y., and Scrutton, N. S. (2001) Two-iron rubredoxin of *Pseudomonas oleovorans*: production, stability and characterization of the individual iron-binding domains by optical, CD, and NMR spectroscopies. *Biochem. J. 354*, 89−98.
21. May, S. W., Lee, L. G., Katopodis, A. G., Kuo, J.-Y., Wimalasena, K., and Thowsen, J. R. (1984) Rubredoxin from *Pseudomonas oleovorans*: effects of selective chemical modification and metal substitution. *Biochemistry 23*, 2187−2192.
22. Henehan, C. J., Pountney, D. L., Zerbe, O., and Vasak, M. (1993) Identification of cysteine ligands in metalloproteins using optical and NMR spectroscopy: cadmium-substituted rubredoxin as a model $[Cd(CysS)_4]_2$- center. *Protein Sci. 2*, 1756−1764.
23. Lee, H. J., Lian, L. Y., and Scrutton, N. S. (1997) Recombinant two-iron rubredoxin of *Pseudomonas oleovorans*: overexpression, purification and characterization by optical, CD, and ^{113}Cd NMR spectroscopies. *Biochem. J. 328*, 131−136.
24. Ueda, T., and Coon, M. J. (1972) Enzymatic oxidation. VII. Reduced diphosphopyridine nucleotide-rubredoxin reductase: properties and function as an electron carrier in hydroxylation. *J. Biol. Chem. 247*, 5010−5016.
25. Lode, E. T., and Coon, M. J. (1971) Enzymatic omega-oxidation. V. Forms of Pseudomonas oleovorans rubredoxin containing one or two iron atoms: structure and function in omega-hydroxylation. *J. Biol. Chem. 246*, 791−802.
26. Nilges, M., Macias, M. J., O'Donoghue, S. I., and Oschkinat, H. (1997) Automated NOESY interpretation with ambiguous distance restraints: the refined NMR solution structure of the pleckstrin homology domain from beta-spectrin. *J. Mol. Biol. 269*, 408−422.
27. Pascual, J., Pfuhl, M., Walther, D., Saraste, M., and Nilges, M. (1997) Solution structure of the spectrin repeat: a left-handed antiparallel triple-helical coiled-coil. *J. Mol. Biol. 273*, 740−751.
28. Sali, A., and Blundell, T. L. (1993) Comparative protein modelling by satisfaction of spatial restraints. *J. Mol. Biol. 234*, 779−815.
29. Linge, J. P., Williams, M. A., Spronk, C. A., Bonvin, A. M., and Nilges, M. (2003) Refinement of protein structures in explicit solvent. *Proteins 50*, 496−506.
30. Laskowski, R. A., Rullmannn, J. A., MacArthur, M. W., Kaptein, R., and Thornton, J. M. (1996) AQUA and PROCHECK-NMR: programs for checking the quality of protein structures solved by NMR. *J. Biomol. NMR 8*, 477−486.
31. Grossmann, J. G., Crawley, J. B., Strange, R. W., Patel, K. J., Murphy, L. M., Neu, M., Evans, R. W., and Hasnain, S. S. (1998) The nature of ligand-induced conformational change in transferrin in solution. An investigation using X-ray scattering, XAFS and site-directed mutants. *J. Mol. Biol. 279*, 461−472.
32. Semenyuk, A. V., and Svergun, D. I. (1991) GNOM − a program package for small-angle scattering data processing. *J. Appl. Crystallogr. 24*, 537−540.
33. Porod, G. (1951) Die Röntgenkleinwinkelstreuung von dichtgepackten kolloiden Systemen I. Teil. *Kolloid Z. 124*, 83−114.
34. Feigin, L. A., and Svergun, D. I. (1987) *Structure Analysis by Small-Angle X-ray and Neutron Scattering*, Plenum Press, New York.
35. Kozin, M. B., and Svergun, D. I. (2001) Automated matching of high- and low-resolution structural models. *J. Appl. Crystallogr. 34*, 33−41.
36. Wuthrich, K. (1986) *NMR of Proteins and Nucleic Acids*, Wiley and Sons, New York.
37. Blake, P. R., Park, J. B., Bryant, F. O., Aono, S., Magnuson, J. K., Eccleston, E., Howard, J. B., Summers, M. F., and Adams, M. W. (1991) Determinants of protein hyperthermostability: purification and amino acid sequence of rubredoxin from the hyperthermophilic archaebacterium *Pyrococcus furiosus* and secondary structure of the zinc adduct by NMR. *Biochemistry 30*, 10885−10895.
38. Baleja, J. D., Thanabal, V., and Wagner, G. (1997) Refined solution structure of the DNA-binding domain of GAL4 and use of 3J(^{113}Cd,^{1}H) in structure determination. *J. Biomol. NMR 10*, 397−401.
39. Blake, P. R., Day, M. W., Hsu, B. T., Joshua-Tor, L., Park, J. B., Hare, D. R., Adams, M. W., Rees, D. C., and Summers, M. F. (1992) Comparison of the X-ray structure of native rubredoxin from *Pyrococcus furiosus* with the NMR structure of the zinc-substituted protein. *Protein Sci. 1*, 1522−1525.
40. Kok, M., Oldenhuis, R., van der Linden, M. P., Meulenberg, C. H., Kingma, J., and Witholt, B. (1989) The *Pseudomonas oleovorans* alkBAC operon encodes two structurally related rubredoxins and an aldehyde dehydrogenase. *J. Biol. Chem. 264*, 5442−5451.
41. van Beilen, J. B., Neuenschwander, M., Smits, T. H., Roth, C., Balada, S. B., and Witholt, B. (2002) Rubredoxins involved in alkane oxidation. *J. Bacteriol. 184*, 1722−1732.
42. Page, C. C., Moser, C. C., Chen, X., and Dutton, P. L. (1999) Natural engineering principles of electron tunnelling in biological oxidation−reduction. *Nature 402*, 47−52.
43. Brunger, A. (1992) X-PLOR 3.1. A system for X-ray crystallography and NMR, Yale University Press, New Haven.

BI035817U